


**Quantum transport in a compensated semimetal  $W_2As_3$  with nontrivial  $Z_2$  indices**Yupeng Li,<sup>1,2</sup> Chenchao Xu,<sup>1</sup> Mingsong Shen,<sup>3</sup> Jinhua Wang,<sup>3</sup> Xiaohui Yang,<sup>1</sup> Xiaojun Yang,<sup>4</sup> Zengwei Zhu,<sup>3</sup> Chao Cao,<sup>5,\*</sup> and Zhu-An Xu<sup>1,2,6,†</sup><sup>1</sup>*Department of Physics, Zhejiang University, Hangzhou 310027, People's Republic of China*<sup>2</sup>*State Key Laboratory of Silicon Materials, Zhejiang University, Hangzhou 310027, People's Republic of China*<sup>3</sup>*Wuhan National High Magnetic Field Center, School of Physics, Huazhong University of Science and Technology, Wuhan 430074, People's Republic of China*<sup>4</sup>*School of Physics and Optoelectronics, Xiangtan University, Xiangtan 411105, People's Republic of China*<sup>5</sup>*Department of Physics, Hangzhou Normal University, Hangzhou 310036, People's Republic of China*<sup>6</sup>*Collaborative Innovation Centre of Advanced Microstructures, Nanjing 210093, People's Republic of China* (Received 17 February 2018; revised manuscript received 15 August 2018; published 24 September 2018)

We report a topological semimetal  $W_2As_3$  with a space group  $C2/m$ . Based on the first-principles calculations, band crossings are partially gapped when spin-orbit coupling is included. The  $Z_2$  indices at the electron filling are [1;111], characterizing a strong topological insulator and topological surface states. From the magnetotransport measurements, nearly quadratic field dependence of magnetoresistance (MR) ( $B \parallel [200]$ ) at 3 K indicates an electron-hole compensated compound whose longitudinal MR reaches 11 500% at 3 K and 15 T. In addition, multiband features are detected from the high-magnetic-field Shubnikov–de Haas (SdH) oscillation, Hall resistivity, and band calculations. A nontrivial  $\pi$  Berry's phase is obtained, suggesting the topological feature of this material. A two-band model can fit well the conductivity and Hall coefficient. Our experiments manifest that the transport properties of  $W_2As_3$  are in good agreement with the theoretical calculations.

DOI: [10.1103/PhysRevB.98.115145](https://doi.org/10.1103/PhysRevB.98.115145)**I. INTRODUCTION**

The research of new topological phases such as topological insulator (TI), topological superconductor, and topological semimetal (TSM) is a hot spot in recent years in condensed matter physics. Among them, topological semimetals are widely studied because there are many types, including Dirac semimetals [1,2], Weyl semimetals [3], nodal-line semimetals [4–9], and semimetals with triply degenerate nodal points [10–12]. In addition, they are closely related to other topological phases and are thus believed to be intermediate states of topological phase transitions [13,14]. These topological semimetals usually exhibit large magnetoresistance and topological surface states. Apart from these topological phases, another kind of topological materials are  $Z_2$  topological metals [15], which are characterized by nontrivial  $Z_2$  topological invariants, topological surface states, and lack of a bulk energy gap, such as the  $LaX$  ( $X = P, As, Sb, Bi$ ) [16] family. Among this family,  $LaBi$  is the only one with topological nontrivial band dispersion proved by angle-resolved photoemission spectroscopy (ARPES) measurements [15].

Recently, transition-metal dipnictides  $MPn_2$  ( $M = Nb$  or  $Ta$ ;  $Pn = As$  or  $Sb$ ) with  $C2/m$  structure have attracted great attention because of extremely large magnetoresistance (XMR), negative magnetoresistance, and other interesting properties [17–23]. According to the theoretical calculations, type-II Weyl points could be induced by magnetic field in

$MPn_2$  [24]. Moreover, a superconducting transition has been observed in  $NbAs_2$  at high pressure [25], and the maximal  $T_c$  is 2.63 K under 12.8 GPa. What is very interesting is that the  $C2/m$  structure remains up to 30 GPa, and thus the topological phase could exist in the superconducting state and it may be a candidate of topological superconductors.  $MoAs_2$  is another compound with  $C2/m$  structure possessing quadratic XMR [26,27], whose XMR may originate from the open-orbit topology [27] instead of the electron-hole compensation in  $MPn_2$ .

These interesting properties in the compounds with  $C2/m$  structure have attracted much research attention. Here we report on a topological material  $W_2As_3$  with  $C2/m$  structure and nontrivial  $Z_2$  indices [1:111] which belongs to a strong TI family [5,9,28–30]. Large MR =  $[R(B) - R(0)]/R(0)$  of approximately 11 500% at 3 K and 15 T is observed in this electron-hole compensated system. Evident quantum oscillations have been observed by using a high pulse magnetic field, from which nine intrinsic frequencies are obtained from the fast Fourier transform (FFT) spectrum, and a nontrivial  $\pi$  Berry's phase can be detected from  $F_{h3}$ ,  $F_{h4}$ , and  $F_{h5}$ . The multiband character is also revealed from both band calculations as well as Hall resistivity measurements. Negative Hall resistivity indicates that this compound is an electron-dominated semimetal. A simple two-band model is proposed to explain the temperature dependence of the Hall coefficient, with which the Hall conductivity and longitudinal conductivity can be well fitted. The Hall coefficient obtained from the fitting data is in agreement with the experimental value of  $R_H$ . All of these illustrate relatively consistent transport behavior and the reliable two-band fitting.

\* ccao@hznu.edu.cn

† zhuan@zju.edu.cn

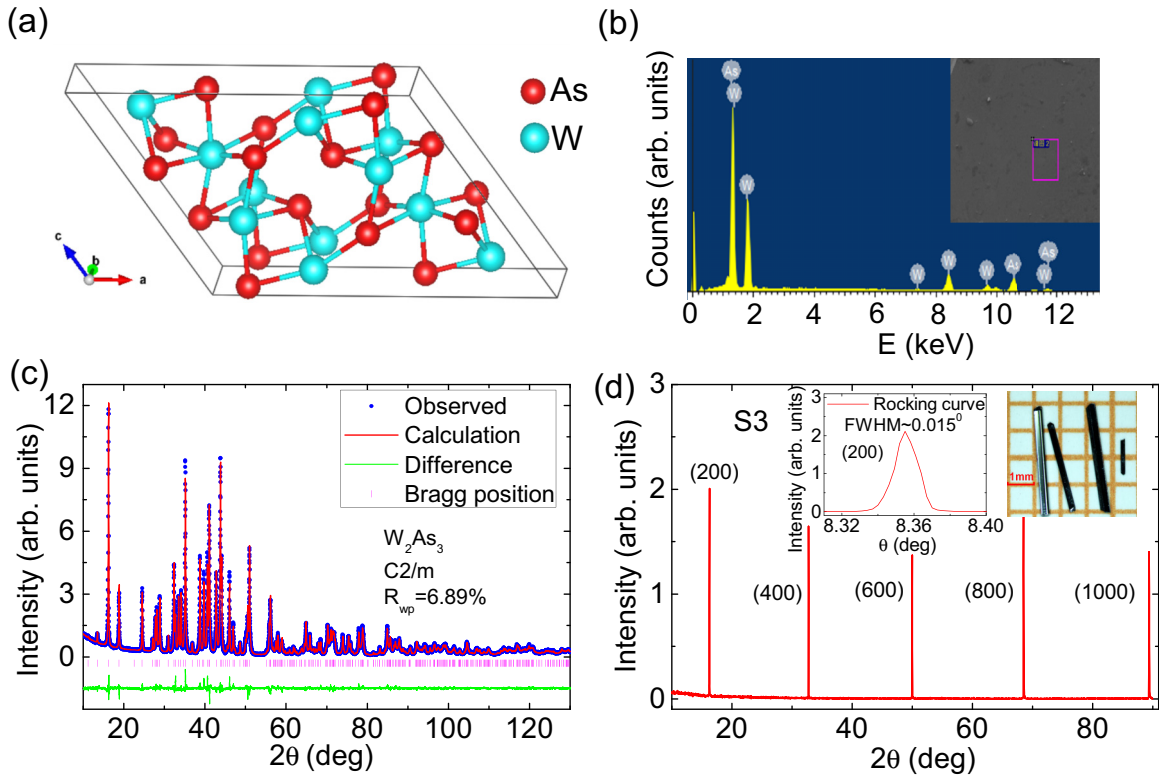


FIG. 1. (a) Crystalline structure of  $W_2As_3$ . (b) EDS spectrum of  $W_2As_3$  and the inset is a scanning electron microscopy figure. (c) Powder XRD pattern of polycrystalline  $W_2As_3$  and Rietveld analysis profiles. (d) XRD pattern of high-quality single crystal showing sharp diffraction peaks of the (200) plane. The left inset is the rocking curve of the (200) peak, and the right inset is a photograph of  $W_2As_3$  crystals.

## II. EXPERIMENT

Single crystals of  $W_2As_3$  were synthesized by an iodine-vapor transport method. Firstly, polycrystalline  $W_2As_3$  was prepared by heating the mixture of W powder and As powder with a stoichiometric ratio of 2:3 at 1173 K for 2 days. Then iodine with a concentration of  $10 \text{ mg/cm}^3$  was mixed with the reground polycrystalline  $W_2As_3$ , and they were sealed in an ampoule to grow single crystals for 7 days in a two-zone furnace, where the temperature gradient was set as 1323–1223 K over a distance of 16 cm. All the experimental processes were carried out in a glove box filled with pure Ar, except the heating processes.

X-ray diffraction (XRD) data were collected by a PANalytical x-ray diffractometer (Empyrean) with a  $Cu K_{\alpha 1}$  radiation. We used energy-dispersive x-ray spectroscopy (EDS) to analyze the composition ratio of W and As element. Longitudinal resistivity and Hall resistivity was measured by a standard six-probe technique. Transport measurements below 15 T were performed on an Oxford-15T cryostat, and a pulsed magnetic field up to 60 T was employed to obtain apparent quantum oscillations in the Wuhan National High Magnetic Field Center (WHMFC - Wuhan).

The first-principles calculations were performed with Vienna *Ab Initio* Simulation Package (VASP) [31,32]. A plane-wave basis up to 400 eV was employed in the calculations. Throughout the calculation, the atom relaxation was performed with the Perdew-Burke-Ernzerhof (PBE) exchange correlation functional, and the electronic band structures,

Fermi surfaces, and surface states were obtained with the modified Becke-Johnson (mBJ) method [33]. A  $\Gamma$ -centred  $15 \times 15 \times 6$  Monkhorst-Pack [34]  $k$ -point mesh was chosen to sample the Brillouin zone for the calculation. The crystal structure was fully optimized until the force on each atom was less than  $1 \text{ meV/\AA}$  and internal stress less than 0.1 kbar. The calculated lattice constants as well as the atomic coordinates were within a 5% error bar compared to the refinement results of XRD data by the software RIETAN-FP [35]. The topological indices  $Z_2$  were calculated by the method of parity check [28]. Using the maximally localized Wannier function method [36], the Fermi surfaces were obtained with a tight-binding Hamiltonian fitted from density functional theory (DFT) bands. The surface states were calculated using a surface Greens function [37].

## III. RESULTS

The crystal structure (a unit cell) of  $W_2As_3$  is presented in Fig. 1(a) with the monoclinic  $C2/m$  (space group no. 12), which has the same space group with  $NbAs_2$  [17–19,22,27,38]. EDS data in Fig. 1(b) give the chemical component ratio  $W:As = 2:2.85$ , consistent with the nominal ratio of 2:3 within the experiment error. Rietveld refinement of powder XRD is fairly reliable with  $R_{wp} = 6.89\%$ , as shown in Fig. 1(c). The refined lattice parameters at room temperature are  $a = 13.322 \text{ \AA}$ ,  $b = 3.277 \text{ \AA}$ ,  $c = 9.593 \text{ \AA}$  and  $\beta = 124.704^\circ$ , which are almost the same as in the previous report [39]. Subsequently, a single-crystal XRD pattern of

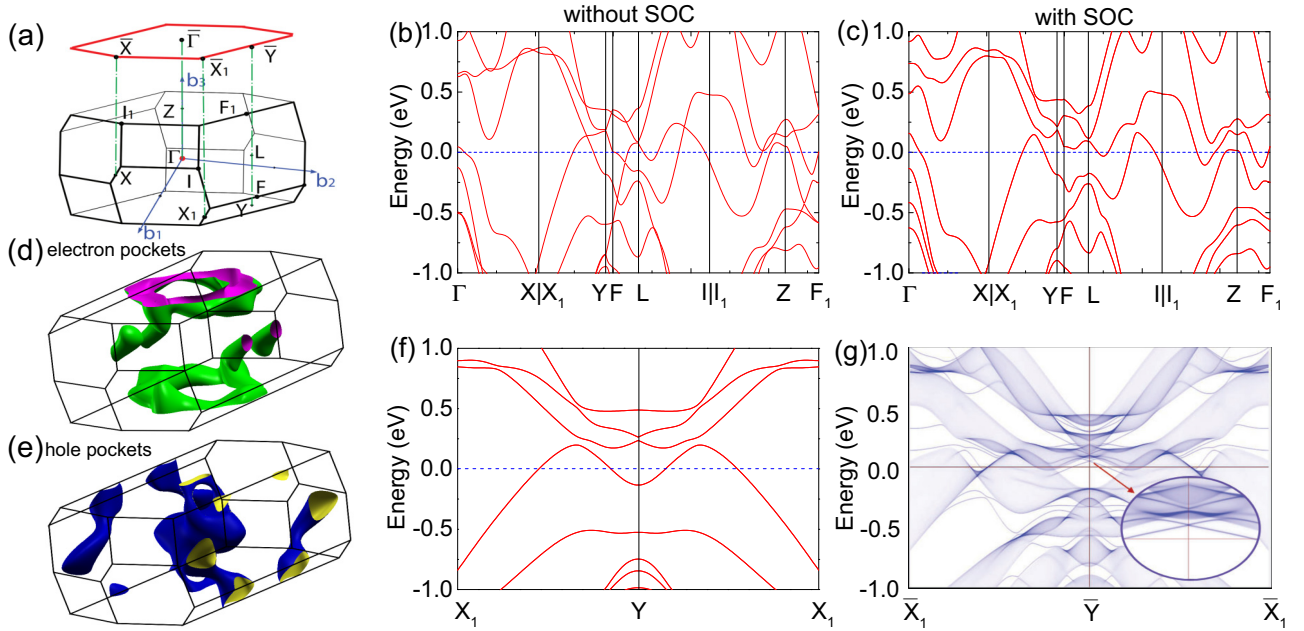


FIG. 2. (a) A schematic diagram of primitive Brillouin zone and the corresponding projection of the (001) surface Brillouin zone. (b) Band structure of  $W_2As_3$  without SOC. (c) The band structure with SOC. (d, e) The 3D Fermi surfaces of electron pockets (green ones) and hole pockets (blue ones) with SOC, respectively. (f) Expanded view of bulk band structure with SOC along  $Y-X_1$ . (g) Calculated (001) surface band structure along the  $\bar{X}_1 - \bar{Y} - \bar{X}_1$  line, and the inset shows the topological surface state.

sample S3 is shown in Fig. 1(d), and the rocking curve in the left inset indicates a high-quality sample (S3) with a small  $\text{FWHM} = 0.015^\circ$  [40]. The obtained single-crystal samples are usually needle-shaped, as shown in the inset of Fig. 1(d).

The band structures of  $W_2As_3$  without and with spin-orbit coupling (SOC) are shown in Fig. 2, respectively. Like the  $TaSb_2$  compound [38], there is a one-electron band and a one-hole band crossing the Fermi level, indicating the two-band feature of this system.  $W_2As_3$ , however, has large Fermi surfaces (FS) [Figs. 2(d) and 2(e)], and three band-crossing features can be identified near the Fermi level. They are along the  $X_1Y$ , FL, and LI directions, respectively, which all resemble the transition metal dipnictides  $XPn_2$  ( $X = Ta, Nb$ ;  $Pn = P, As, Sb$ ) [38]. Once the SOC is included, all the band crossings are gapped, leaving these two bands separated near the Fermi level  $E_f$ . Therefore this system can be adiabatically deformed to an insulator without closing or opening gaps, thus allowing us to define the  $Z_2$  index with the parity at the time-reversal invariant momenta (TRIM) multiplied up to the highest valence band, similar to the cases of LaBi [15] and CeSb [41]. As both the highest valence band (band 27) and lowest conduction band (band 28) are crossing the Fermi level, we list the band parities up to four bands  $\Pi_{26}$ ,  $\Pi_{27}$ ,  $\Pi_{28}$ , and  $\Pi_{29}$  in Table I, where  $\Pi_n$  is the multiplication of the parities for bands 1 to  $n$ . There are 54 valence electrons in the primitive cell, corresponding to 27 filled bands. The product of parities at all these TRIMs up to the 27th band is  $-1$ , suggesting a strong topological property of this compound. In addition, we also performed the PBE calculations and obtained the same topological properties as the mBJ calculations, in contrast to the divergence between the PBE and mBJ calculations in  $LnPn$  ( $Ln = Ce, Pr, Gd,$

$Sm, Yb$ ;  $Pn = Sb, Bi$ ) [42] and LaSb [43], in which the PBE calculations underestimate the band gap between the conduction band and valence band. Compared with the bulk band structure along  $X_1 - Y$  in Fig. 2(f), we calculate the (001) surface states along  $\bar{X}_1 - \bar{Y} - \bar{X}_1$  as shown in Fig. 2(g). Although there are strong bulk states due to the large hole and electron pockets in Fig. 2(g), the Dirac type of surface states can be still observed at the  $\bar{Y}$  point in the inset of Fig. 2(g).

We now turn to the transport properties of  $W_2As_3$ . The temperature-dependent  $\rho_{xx}$  of different samples S1, S2, and S3 all exhibit a typical metallic behavior, and the corresponding residual resistance ratio [RRR =  $\rho_{xx}(300\text{ K})/\rho_{xx}(1.5\text{ K})$ ] is 291, 311, and 372, respectively. Therefore sample S3 is chosen to perform further studies. The giant MR of about 11500% at 15 T and 3 K is displayed in the inset of Fig. 3(a) without obvious quantum oscillations. The MR can

TABLE I. Parities of bands at time-reversal invariant momenta (TRIM).  $\Pi_n$  is the multiplication of the parities for bands 1 to  $n$ . The highest occupied band at each TRIM is indicated with  $^\circ$ . The corresponding  $Z_2$  classification is [1,111].

TRIM	$\Pi_{26}$	$\Pi_{27}$	$\Pi_{28}$	$\Pi_{29}$
(0,0,0)	$-^\circ$	-	+	-
$(\pi,0,0)$	+	$-^\circ$	-	+
$(0,\pi,0)$	+	$-^\circ$	-	+
$(\pi,\pi,0)$	-	$^\circ$	-	-
$(0,0,\pi)$	$-^\circ$	+	+	+
$(\pi,0,\pi)$	-	$^\circ$	+	+
$(0,\pi,\pi)$	-	$^\circ$	+	+
$(\pi,\pi,\pi)$	-	$^\circ$	-	-

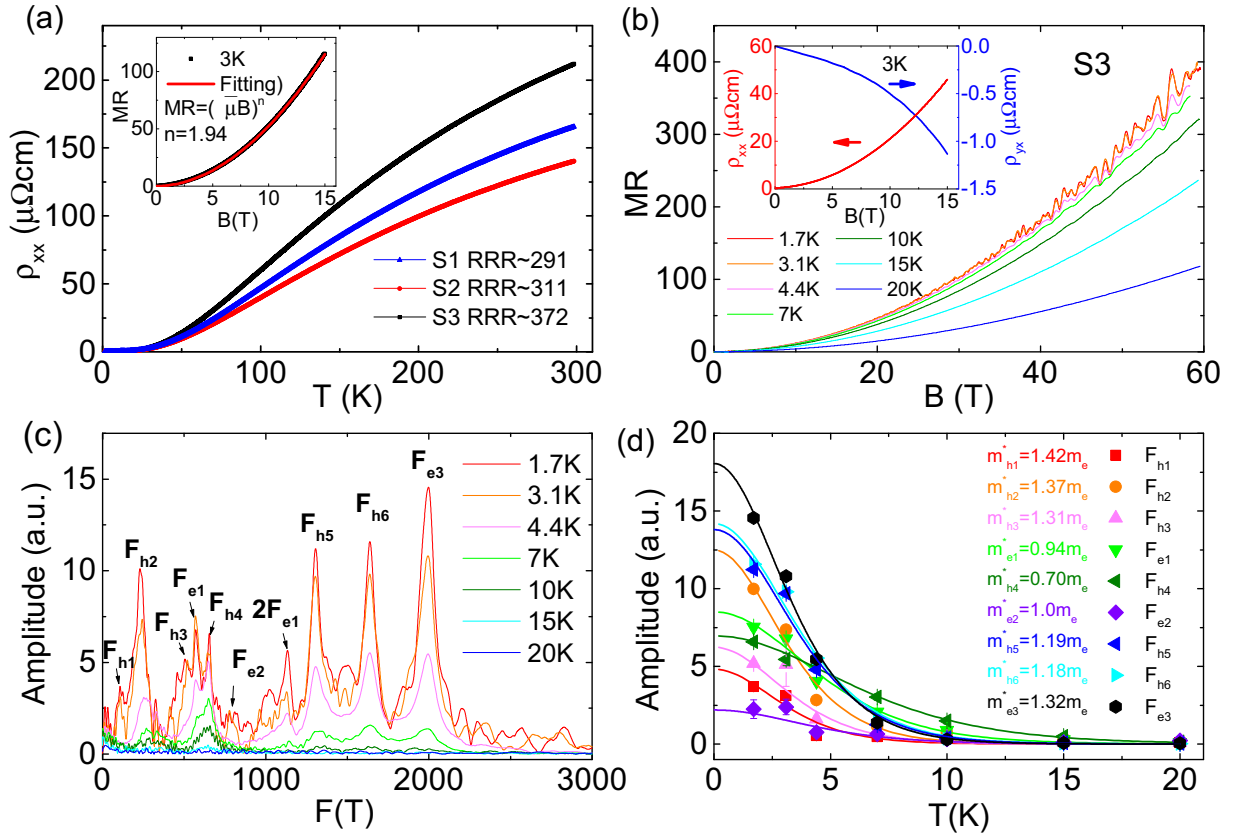


FIG. 3. (a) Temperature-dependent resistivity of several samples. The inset is a fitting result with  $MR = (\bar{\mu}B)^n$ . (b) Visible quantum oscillations under high magnetic field. The inset displays  $\rho_{xx}$  measured up to 15 T, which is much larger than  $\rho_{yx}$ . (c) FFT curves suggesting the nine independent intrinsic frequencies. (d) Fitting the SdH amplitudes by the LK formula. The obtained effective masses of the nine FFT frequencies are shown.

be well fitted by  $MR = (\bar{\mu}B)^n$  with  $n = 1.94$ , indicating good electron-hole compensation [44,45]. The geometric mean of the mobilities is  $\bar{\mu} = \sqrt{\mu_e\mu_h} = 0.72T^{-1}$  when  $n = 2$  is used.

In order to extract more information about the Fermi surface of  $W_2As_3$ , a pulsed magnetic field experiment up to 60 T is performed. In Fig. 3(b), large quantum oscillations in resistance become visible at various temperatures, and no sign of saturation in MR is detected up to 60 T. The inset of Fig. 3(b) shows  $|\rho_{yx}| \ll |\rho_{xx}|$ , so we can use  $\rho_{xx}$  to analyze the quantum oscillation data. After removing the background, nine distinct frequencies of extremal orbits are observed from a complicated FFT spectrum in Fig. 3(c). The calculated frequencies are in good agreement with experimental observations, considering the error between the experimental results and theoretical calculations [46], as shown in Table II. Using the Lifshitz-Kosevich (LK) formula,

$$\Delta R_{xx} \propto R_T \times R_D \times \cos \left[ 2\pi \left( \frac{F}{B} + \gamma - \delta \right) \right], \quad (1)$$

where  $R_T = (2\pi^2 k_B T / \beta) / \sinh(2\pi^2 k_B T / \beta)$ ,  $\beta = e\bar{B}\hbar / m^*$ ,  $k_B$  is Boltzmann constant, and  $\bar{B}$  is the average field value [47,48]. The obtained effective mass  $m^*$  of each pocket is also indicated in Fig. 3(d), where the smallest  $m_{h4}^* = 0.70m_0$  and largest  $m_{h1}^* = 1.42m_0$ . Due to the complicated Fermi surface, as seen in Figs. 2(d) and 2(e), nine filtered oscillatory parts in Figs. 4(b) and 4(c) are detected by the decomposition of  $\Delta\rho_{xx}$

in Fig. 4(a), which is obtained by subtracting the background of  $\rho_{xx}$  at 1.7 K. Although both the messy frequencies and harmonic frequencies are eliminated, the sum of nine main frequencies (blue line) matches the experimental data (red line) very well in Fig. 4(a), both in amplitudes and phases. Therefore we assign the Landau level by the peak position of the oscillation component of each frequency in Figs. 4(b) and 4(c) [49–51]. In the Lifshitz-Onsager (LO) formula,

$$A_n \frac{\hbar}{eB} = 2\pi(n + \gamma - \delta), \quad (2)$$

TABLE II. Physical parameters of nine extremal orbits are listed when magnetic field is along the (200) facet of  $W_2As_3$ .  $m_0$  is the static mass of the electron. The DFT results here are the SdH frequencies from calculated band energies [46].

FS	SdH(T)	$m^*(m_0)$	DFT(T)
$F_{h1}$	106	1.42	58
$F_{h2}$	232	1.37	140
$F_{h3}$	505	1.31	181
$F_{e1}$	574	0.94	577
$F_{h4}$	653	0.70	605
$F_{e2}$	778	1.00	623
$F_{h5}$	1305	1.19	1262
$F_{h6}$	1640	1.18	1460
$F_{e3}$	1997	1.32	1534

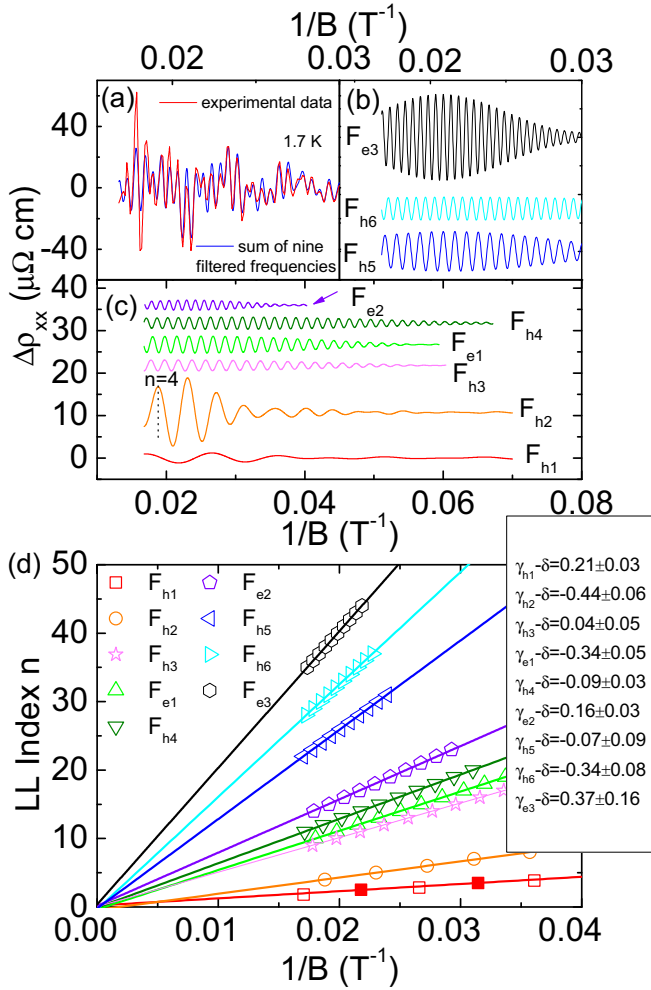


FIG. 4. (a) Oscillatory part of the resistivity ( $\Delta\rho_{xx}$ ) as a function of  $1/B$  at 1.7 K (the red line is experimental data).  $\Delta\rho_{xx}$  is obtained after subtracting the background of  $\rho_{xx}$ . The blue line is the sum of nine filtered frequencies. (b, c) The nine filtered oscillatory parts of  $\Delta\rho_{xx}$ . The Landau-level index is obtained from the peak position of the oscillation component, for example, one of the oscillatory peaks about  $F_{h2}$  is  $n = 4$  in (c). (d) Landau-level index plot of the nine frequencies. The intercepts are between  $-1/8$  and  $1/8$  for  $F_{h3}$ ,  $F_{h4}$ , and  $F_{h5}$ , respectively. Open circles indicate the integer Landau-level index from the peaks of high-frequency oscillatory components of  $\Delta\rho_{xx}$ , and closed circles denote the half-integer index ( $\Delta\rho_{xx}$  valley).

where  $A_n$  is the FS cross section area of the Landau level (LL)  $n$ .  $\gamma - \delta = \frac{1}{2} - \frac{\phi_B}{2\pi} - \delta$  is the phase factor, where  $\phi_B$  is the Berry phase and  $\delta$  is a phase shift induced by dimensionality [ $\delta = 0$  for two dimensions (2D), or  $\delta = \pm\frac{1}{8}$  for three dimensions (3D)]. The Landau-level index is fitted by the LO formula in Fig. 4(d), and we can obtain the intercepts of nine frequencies. Furthermore,  $|\gamma - \delta|$  of  $F_{h3}$ ,  $F_{h4}$ , and  $F_{h5}$  are 0.04, 0.09, and 0.07, respectively, which are all in the range between 0 and  $1/8$ , exhibiting a nontrivial Berry's phase of  $\pi$  [52,53]. Theoretically, when a singularity in the energy band is enclosed by the cyclotron contour under magnetic field, we could detect a nontrivial  $\pi$  Berry's phase from Shubnikov-de Haas (SdH) oscillation [54,55]. It is worth noting that

the observation of a  $\pi$  Berry phase from SdH oscillation is affected by the magnetic field directions and the cross sections of Fermi surfaces; thus some nontrivial Fermi surfaces may not yield exact  $\pi$  Berry phase in SdH measurements [54–56]. For the materials with a complex Fermi surface, some unexpected frequencies, such as low frequencies and harmonic frequencies, would affect the filtered main frequency more or less. For example, the harmonic frequency  $2F_{h4}$  (1306 T) may be mixed into the filtered  $F_{h5}$  (1305 T) and thus modulates the oscillation data of  $F_{h5}$  in Fig. 4(b), which could affect the precise determination of the Berry phase of  $F_{h5}$  in Fig. 4(d).

The measurements of  $\rho_{xx}(B)$  and  $\rho_{yx}(B)$  provide further insight on the transport properties, as seen in Figs. 5(a) and 5(b). The negative  $\rho_{yx}(B)$  shown in Fig. 5(b) indicates that the electron-type carriers play a dominant role in transport properties, and the nonlinear magnetic field dependence implies the multiband feature. Figures 5(c) and 5(d) display that the curves of conductivity  $\sigma_{xx} = \rho_{xx}/(\rho_{xx}^2 + \rho_{yx}^2)$  and  $\sigma_{xy} = \rho_{yx}/(\rho_{xx}^2 + \rho_{yx}^2)$  can be well fitted by the two-band model:

$$\sigma_{xx} = e \left[ \frac{n_h \mu_h}{1 + (\mu_h B)^2} + \frac{n_e \mu_e}{1 + (\mu_e B)^2} \right], \quad (3)$$

$$\sigma_{xy} = eB \left[ \frac{n_h \mu_h^2}{1 + (\mu_h B)^2} - \frac{n_e \mu_e^2}{1 + (\mu_e B)^2} \right], \quad (4)$$

where  $n_e$ ,  $n_h$ ,  $\mu_e$ , and  $\mu_h$  are electron-type carrier density, hole-type carrier density, electron-type mobility, and hole-type mobility, respectively. Both the electron and hole mobility decrease monotonously as temperature increases, as seen in Fig. 5(f), which is a typical behavior for metals. Intriguingly, the electron-hole compensation only holds at low temperatures and becomes ineffective above 50 K. The Hall coefficient obtained by fitting with the two-band model  $R_H = [R_H^h(\sigma_{xx}^h)^2 - R_H^e(\sigma_{xx}^e)^2]/(\sigma_{xx}^h + \sigma_{xx}^e)^2$  [57], as shown in Fig. 5(e), is quite consistent with the directly measured  $R_H$  which is acquired from the slope of  $\rho_{yx}$  near the zero field, where  $R_H^h$  and  $R_H^e$  are the Hall coefficient for hole-type and electron-type charge carriers, respectively,  $\sigma_{xx}^h$  and  $\sigma_{xx}^e$  are the hole conductivity and electron conductivity, respectively, and  $\sigma_{xx} = en\mu$ . All of above fitting results suggest that the two-band model fits the experimental data reliably. It is apparent that the absolute value of  $R_H$  changes little below 14 K and becomes large with increasing temperature, then becomes small again above 100 K, at which temperature the slope of  $\rho_{yx}(B)$  reaches the maximum [Fig. 5(b)]. We propose that the shift of Fermi level with increasing temperature may account for the loss of the electron-hole compensation above 50 K. Similar behavior and explanations were reported in  $\text{WTe}_2$  [58] and  $\text{ZrTe}_5$  [59].

#### IV. CONCLUSION

In summary, we have discovered a topological semimetal  $\text{W}_2\text{As}_3$  with  $Z_2$  indices [1;111] which has a strong TI feature. The electron-hole compensation leads to a colossal MR which is as large as 11 500% at 3 K and 15 T and is unsaturated even up to 60 T. A nontrivial Berry's phase of  $\pi$  is obtained from  $F_{h3}$ ,  $F_{h4}$ , and  $F_{h5}$ , suggesting the nontrivial topological characteristic. A two-band model is effective to fit the Hall

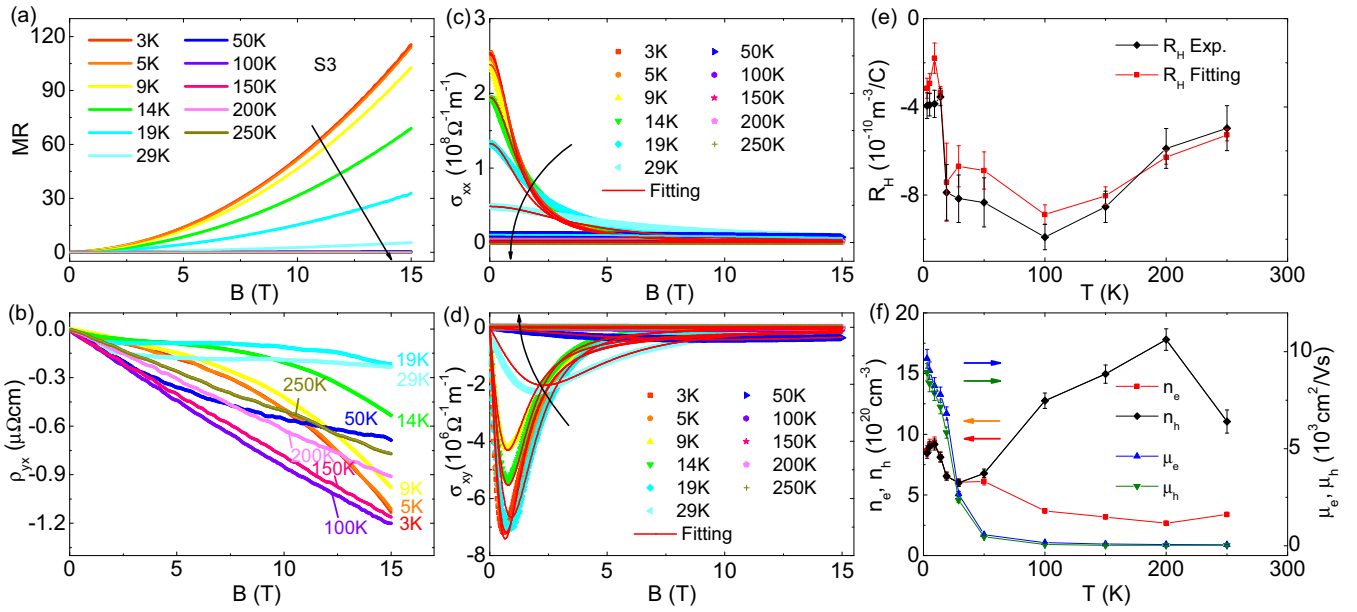


FIG. 5. (a) Magnetoresistance at various temperatures; (b) Hall resistivity vs magnetic field; (c) conductivity  $\sigma_{xx}$  vs magnetic field; (d) Hall conductivity  $\sigma_{xy}$  vs magnetic field; and (e) temperature dependence of Hall coefficient  $R_H$ .  $R_H$  (solid square) obtained from the two-band model fitting is compared with the experimental data of  $R_H$  (diamond). (f) Temperature dependence of  $n_e$ ,  $n_h$ ,  $\mu_e$ , and  $\mu_h$  obtained in the two-band model fitting.

conductivity and Hall coefficient. The transport properties are in good agreement with the band structure calculations.

#### ACKNOWLEDGMENTS

We thank Yi Zhou, Yongkang Luo, and Chenqiang Hua for insightful discussions. This work was supported by the

National Key R&D Program of the China (Grants No. 2016YFA0300402 and No. 2014CB648400), the National Science Foundation of China (Grants No. 11774305 and No. 11274006), and the Fundamental Research Funds for the Central Universities of China.

Y.L. and C.X. contributed equally to this work.

- [1] Z. J. Wang, Y. Sun, X.-Q. Chen, C. Franchini, G. Xu, H. M. Weng, X. Dai, and Z. Fang, *Phys. Rev. B* **85**, 195320 (2012).
- [2] Z. Wang, H. Weng, Q. Wu, X. Dai, and Z. Fang, *Phys. Rev. B* **88**, 125427 (2013).
- [3] H. Weng, C. Fang, Z. Fang, B. A. Bernevig, and X. Dai, *Phys. Rev. X* **5**, 011029 (2015).
- [4] G. Bian, T. R. Chang, R. Sankar, S. Y. Xu, H. Zheng, T. Neupert, C. K. Chiu, S. M. Huang, G. Q. Chang, I. Belopolski, D. S. Sanchez, M. Neupane, N. Alidoust, C. Liua, B. K. Wang, C. C. Lee, H. T. Jeng, C. L. Zhang, Z. J. Yuan, S. Jia *et al.*, *Nat. Commun.* **7**, 10556 (2016).
- [5] R. Yu, H. M. Weng, Z. Fang, X. Dai, and X. Hu, *Phys. Rev. Lett.* **115**, 036807 (2015).
- [6] Y. K. Kim, B. J. Wieder, C. L. Kane, and A. M. Rappe, *Phys. Rev. Lett.* **115**, 036806 (2015).
- [7] Q. N. Xu, Z. D. Song, S. M. Nie, H. M. Weng, Z. Fang, and X. Dai, *Phys. Rev. B* **92**, 205310 (2015).
- [8] C. Fang, Y. G. Chen, H. Y. Kee, and L. Fu, *Phys. Rev. B* **92**, 081201 (2015).
- [9] A. Yamakage, Y. Yamakawa, Y. Tanaka, and Y. Okamoto, *J. Phys. Soc. Jpn.* **85**, 013708 (2016).
- [10] B. Bradlyn, J. Cano, Z. J. Wang, M. G. Vergniory, C. Felser, R. J. Cava, and B. A. Bernevig, *Science* **353**, aaf5037 (2016).
- [11] H. M. Weng, C. Fang, Z. Fang, and X. Dai, *Phys. Rev. B* **93**, 241202 (2016).
- [12] B. Q. Lv, Z.-L. Feng, Q.-N. Xu, X. Gao, J.-Z. Ma, L.-Y. Kong, P. Richard, Y.-B. Huang, V. N. Strocov, C. Fang, H.-M. Weng, Y.-G. Shi, T. Qian, and H. Ding, *Nature (London)* **546**, 627 (2017).
- [13] Z. K. Liu, B. Zhou, Y. Zhang, Z. J. Wang, H. M. Weng, D. Prabhakaran, S.-K. Mo, Z. X. Shen, Z. Fang, X. Dai, Z. Hussain, and Y. L. Chen, *Science* **343**, 864 (2014).
- [14] X. G. Wan, A. M. Turner, A. Vishwanath, and S. Y. Savrasov, *Phys. Rev. B* **83**, 205101 (2011).
- [15] J. Nayak, S.-C. Wu, N. Kumar, C. Shekhar, S. Singh, J. Fink, E. E. D. Rienks, G. H. Fecher, S. S. P. Parkin, B. Yan, and C. Felser, *Nat. Commun.* **8**, 13942 (2017).
- [16] M. G. Zeng, C. Fang, G. Chang, Y.-A. Chen, T. Hsieh, A. Bansil, H. Lin, and L. Fu, *arXiv:1504.03492*.
- [17] Y. K. Li, L. Li, J. L. Wang, T. T. Wang, X. F. Xu, C. Y. Xi, C. Cao, and J. H. Dai, *Phys. Rev. B* **94**, 121115(R) (2016).
- [18] Y. P. Li, Z. Wang, Y. H. Lu, X. J. Yang, Z. X. Shen, F. Sheng, C. M. Feng, Y. Zheng, and Z.-A. Xu, *arXiv:1603.04056*.
- [19] B. Shen, X. Y. Deng, G. Kotliar, and N. Ni, *Phys. Rev. B* **93**, 195119 (2016).
- [20] D. Wu, J. Liao, W. Yi, X. Wang, P. Li, H. Weng, Y. Shi, Y. Li, J. Luo, X. Dai, and Z. Fang, *Appl. Phys. Lett.* **108**, 042105 (2016).

- [21] Y. K. Luo, R. D. McDonald, P. F. S. Rosa, B. Scott, N. Wakeham, N. J. Ghimire, E. D. Bauer, J. D. Thompson, and F. Ronning, *Sci. Rep.* **6**, 27294 (2016).
- [22] Z. J. Yuan, H. Lu, Y. J. Liu, J. F. Wang, and S. Jia, *Phys. Rev. B* **93**, 184405 (2016).
- [23] Y.-Y. Wang, Q.-H. Yu, P.-J. Guo, K. Liu, and T.-L. Xia, *Phys. Rev. B* **94**, 041103(R) (2016).
- [24] D. Gresch, Q. Wu, G. W. Winkler, and A. A. Soluyanov, *New J. Phys.* **19**, 035001 (2017).
- [25] Y. P. Li, C. An, C. Q. Hua, X. L. Chen, Y. H. Zhou, Y. Zhou, R. R. Zhang, C. Y. Park, Z. Wang, Y. H. Lu, Y. Zheng, Z. R. Yang, and Z. A. Xu (unpublished).
- [26] J. Wang, L. Li, W. You, T. Wang, C. Cao, J. Dai, and Y. Li, *Sci. Rep.* **7**, 15669 (2017).
- [27] R. Lou, Y. F. Xu, L.-X. Zhao, Z.-Q. Han, P.-J. Guo, M. Li, J.-C. Wang, B.-B. Fu, Z.-H. Liu, Y.-B. Huang, P. Richard, T. Qian, K. Liu, G.-F. Chen, H. M. Weng, H. Ding, and S.-C. Wang, *Phys. Rev. B* **96**, 241106(R) (2017).
- [28] L. Fu and C. L. Kane, *Phys. Rev. B* **76**, 045302 (2007).
- [29] J. C. Y. Teo, L. Fu, and C. L. Kane, *Phys. Rev. B* **78**, 045426 (2008).
- [30] M. Z. Hasan and C. L. Kane, *Rev. Mod. Phys.* **82**, 3045 (2010).
- [31] G. Kresse and J. Hafner, *Phys. Rev. B* **47**, 558 (1993).
- [32] G. Kresse and J. Furthmüller, *Phys. Rev. B* **54**, 11169 (1996).
- [33] F. Tran and P. Blaha, *Phys. Rev. Lett.* **102**, 226401 (2009).
- [34] H. J. Monkhorst and J. D. Pack, *Phys. Rev. B* **13**, 5188 (1976).
- [35] F. Izumi and K. Momma, *Solid State Phenom.* **130**, 15 (2007).
- [36] I. Souza, N. Marzari, and D. Vanderbilt, *Phys. Rev. B* **65**, 035109 (2001).
- [37] M. P. Lopez Sancho, J. M. Lopez Sancho, J. M. L. Sancho, and J. Rubio, *J. Phys. F: Met. Phys.* **15**, 851 (1985).
- [38] C. C. Xu, J. Chen, G.-X. Zhi, Y. K. Li, J. H. Dai, and C. Cao, *Phys. Rev. B* **93**, 195106 (2016).
- [39] J. B. Taylor, L. D. Calvert, and M. R. Hunt, *Can. J. Chem.* **43**, 3045 (1965).
- [40] H. Xing, G. Long, H. J. Guo, Y. M. Zou, C. M. Feng, G. H. Cao, H. Zeng, and Z.-A. Xu, *J. Phys.: Condens. Matter* **23**, 216005 (2011).
- [41] C. Guo, C. Cao, M. Smidman, F. Wu, Y. Zhang, F. Steglich, F.-C. Zhang, and H. Yuan, *npj Quantum Mater.* **2**, 39 (2017).
- [42] X. Duan, F. Wu, J. Chen, P. Zhang, Y. Liu, H. Yuan, and C. Cao, [arXiv:1802.04554](https://arxiv.org/abs/1802.04554).
- [43] P.-J. Guo, H.-C. Yang, B.-J. Zhang, K. Liu, and Z.-Y. Lu, *Phys. Rev. B* **93**, 235142 (2016).
- [44] M. N. Ali, J. Xiong, S. Flynn, J. Tao, Q. D. Gibson, L. M. Schoop, T. Liang, N. Haldolaarachchige, M. Hirschberger, N. P. Ong, and R. J. Cava, *Nature (London)* **514**, 205 (2014).
- [45] Z. W. Zhu, X. Lin, J. Liu, B. Fauqué, Q. Tao, C. L. Yang, Y. G. Shi, and K. Behnia, *Phys. Rev. Lett.* **114**, 176601 (2015).
- [46] P. M. C. Rourke and S. R. Julian, *Comput. Phys. Commun.* **183**, 324 (2012).
- [47] D. Rhodes, S. Das, Q. R. Zhang, B. Zeng, N. R. Pradhan, N. Kikugawa, E. Manousakis, and L. Balicas, *Phys. Rev. B* **92**, 125152 (2015).
- [48] S. S. Sun, Q. Wang, P.-J. Guo, K. Liu, and H. C. Lei, *New J. Phys.* **18**, 082002 (2016).
- [49] J. Hu, Z. J. Tang, J. Y. Liu, Y. L. Zhu, J. Wei, and Z. Q. Mao, *Phys. Rev. B* **96**, 045127 (2017).
- [50] M. Matusiak, J. R. Cooper, and D. Kaczorowski, *Nat. Commun.* **8**, 15219 (2017).
- [51] A. A. Taskin and Y. Ando, *Phys. Rev. B* **80**, 085303 (2009).
- [52] K. S. Novoselov, A. K. Geim, S. V. Morozov, D. Jiang, M. I. Katsnelson, I. V. Grigorieva, S. V. Dubonos, and A. A. Firsov, *Nature (London)* **438**, 197 (2005).
- [53] Y. B. Zhang, Y.-W. Tan, H. L. Stormer, and P. Kim, *Nature (London)* **438**, 201 (2005).
- [54] G. P. Mikitik and Y. V. Sharlai, *Phys. Rev. Lett.* **82**, 2147 (1999).
- [55] Z. J. Xiang, D. Zhao, Z. Jin, C. Shang, L. K. Ma, G. J. Ye, B. Lei, T. Wu, Z. C. Xia, and X. H. Chen, *Phys. Rev. Lett.* **115**, 226401 (2015).
- [56] C. Li, C. M. Wang, B. Wan, X. Wan, H.-Z. Lu, and X. C. Xie, *Phys. Rev. Lett.* **120**, 146602 (2018).
- [57] F. Rullier-Albenque, D. Colson, A. Forget, and H. Alloul, *Phys. Rev. Lett.* **103**, 057001 (2009).
- [58] Y. Wu, N. H. Jo, M. Ochi, L. Huang, D. Mou, S. L. Bud'ko, P. C. Canfield, N. Trivedi, R. Arita, and A. Kaminski, *Phys. Rev. Lett.* **115**, 166602 (2015).
- [59] Y. Zhang, C. Wang, L. Yu, G. Liu, A. Liang, J. Huang, S. Nie, X. Sun, Y. Zhang, B. Shen, J. Liu, H. Weng, L. Zhao, G. Chen, X. Jia, C. Hu, Y. Ding, W. Zhao, Q. Gao, C. Li *et al.*, *Nat. Commun.* **8**, 15512 (2017).